Aspherical surface measurement: a cost-effective and fast AI solution

Gaston Baudat[1], Robert E. Parks[2]

[1]Innovations Foresight, LLC., 4432 Mallard Point, Columbus Indiana, IN. 47201, USA
[1]Adjunct Research Professor, Wyant College of Optical Sciences, The University of Arizona, 1630 E. University Blvd., Tucson, Arizona 85721, USA
[2]Optical Perspectives Group, LLC. 7011 E. Calle Tolosa, Tucson, AZ 85750, USA

Abstract

Optical aspherical surfaces have become more widely used as they offer advantages such as improved image quality, compact design, increased light gathering, and reduced distortion. However, measuring aspherical surfaces presents challenges due to their non-spherical shapes. The primary difficulties include the complexity of surface geometries and the need for specialized metrology equipment. These challenges require advanced measurement techniques to ensure accurate characterization and quality control of aspherical surfaces in various applications. This paper introduces an innovative, AI-driven solution for the measurement of aspherical surfaces within the image space, offering a flexible optical metrology tool for measuring aspherical surfaces. This approach is characterized by its ability to deliver rapid and cost-effective integration without the need for custom, complex optics.

1. INTRODUCTION

Image space wavefront sensing (IS-WFS) techniques are methods for determining an optical wavefront directly from image data, without the need for specialized wavefront sensors or interferometers. These techniques belong to the field of computational optics leveraging image processing algorithms to interpret the phase information encoded in images, offering a flexible and potentially cost-effective alternative to traditional wavefront sensing methods.

Typical IS-WFS approaches include:

1. **Phase Retrieval**: This method reconstructs the wavefront phase by iteratively refining a model to match the observed image, often using algorithms such as Gerchberg-Saxton or hybrid input-output methods.
2. **Phase Diversity**: Involves capturing multiple images with known aberrations (typically, defocus) and jointly solving for the wavefront phase that explains all observed images.
3. **Curvature Sensing (CS)**: Although the methods described in 1 and 2 are non-parametric by nature, CS is a parametric approach solving the irradiance transport equation. It has been successfully applied by Roddier and Roddier [1] in the context of adaptive optics (AO) in astronomy.

The main advantages of IS-WFS include its ability to integrate seamlessly with existing imaging systems and the elimination of the need for additional wavefront sensing hardware. This makes IS-WFS particularly attractive for applications where space, weight, and cost constraints are critical, such as in space telescopes and portable optical devices. The absence of a reference beam and interference significantly simplified the system, making it more robust to vibrations, noise and turbulence. Challenges remain, particularly in managing the computational load required for real-time processing. Figure 1 below summarizes the basic approaches described above.
Machine learning offers yet another approach for IS-WFS. Unlike traditional ones there is no need for time consuming iterative processing for solving and retrieving the wavefront from images at run time. Typically, an artificial neural network (NN) is used to learn the inverse function relating the image (irradiance) to the wavefront (the phase). On the other hand, single image WF sensing using phase retrieval algorithms from a known source typically relies on iterative error reduction techniques, such as the Gerchberg-Saxton (GS) algorithm. The GS algorithm convergence tends to be rather slow, typically characterized by plateaus where the error remains almost constant across many iterations. Iterative joint maximum a posteriori estimation procedure in phase diversity (multiple images) and Poisson solvers for CS often yields approximations rather than exact solutions, with accuracy dependent on initial conditions.

Optical Manufacturing and Testing 2024, edited by Daewook Kim, Heejoo Choi, Heidi Ottevaere, Proc. of SPIE Vol. 13134, 1313403 · © 2024 SPIE
0277-786X · doi: 10.1117/12.3027354

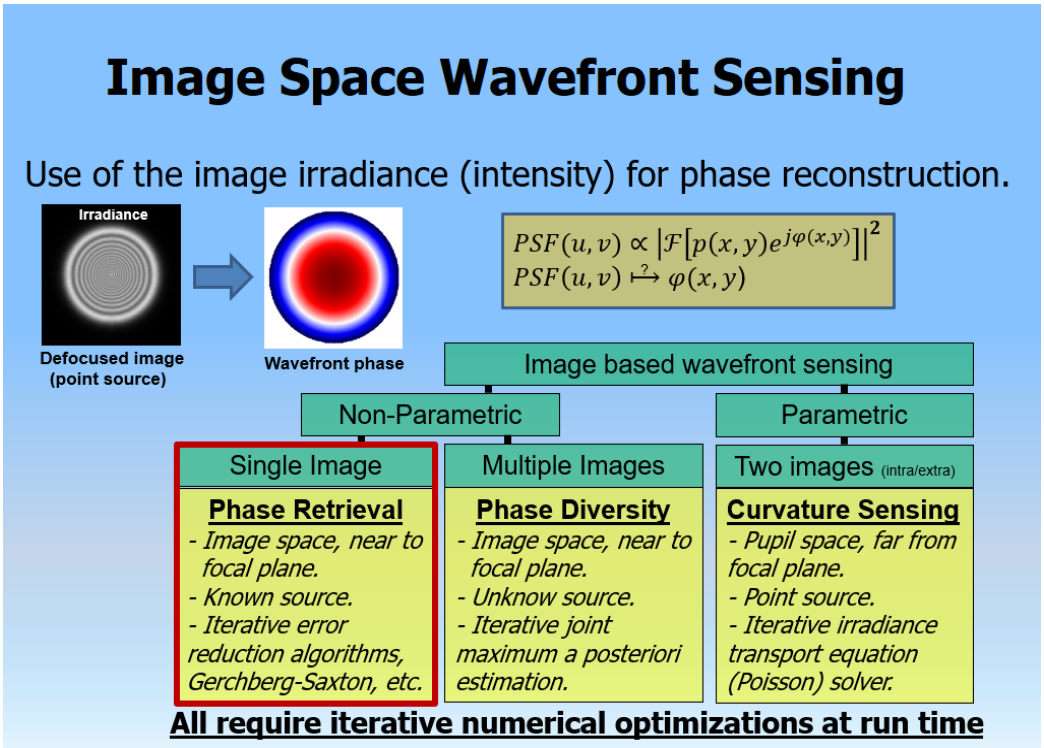

Figure 1. Common approaches used in the context for image space wavefront sensing

Baudat introduced an IS-WFS approach using artificial intelligence [2], capable of performing phase retrieval from a single defocused image, even under noisy conditions. This patented method, known as AI4Wave, exibits four highly desirable features:

- Requires only a single image.
- Training and validation using only synthetic (simulated) data.
- Fast processing (no iteration) at run time.
- Whole field WF sensing.

An artificial neural network (NN) forms the core of the AI4Wave method and is trained solely on synthetic data, which is a key feature of this approach, allowing for the creation of arbitrarily large training and validation databases for accurately sampling this inverse function problem. The data consists of simulated aberrated and defocused images. By design, the NN processes normalized images to be as agnostic as possible to basic system parameters, such as wavelength, aperture, focal length, and pixel size. This enables a single NN to be used across a wide range of applications without requiring new training; the images are just normalized before presented to the NN. The AI4Wave was first implemented in the context of telescope alignment and active optics in astronomy. Since then, it has been applied in optical metrology, seamlessly integrating into the Point Source Microscope (PSM) for the Optical Perspectives Group [4].

The simulated images are computed using scalar diffraction theory. The NN serves as a function approximation tool, mapping single defocused images to their respective wavefronts, commonly expressed in Zernike annular polynomial coefficients. As a result, during runtime, there is no need for iterations, optimizations, or concerns about convergence for phase retrieval calculations. All the complex computations have been carried out during the training phase of the NN. When presented with a new single-defocused image of a star, the NN provides the related wavefront data (i.e., the Zernike

annular polynomial coefficients). The chosen NN's feed-forward structure enables fast phase retrieval calculations, aligning well with video-rate wavefront sensing applications.

Inherently, this method can access wavefronts in the entire field simultaneously when presented with a single defocused star field image (artificial or natural). For the scope of this paper, we consider only monochromatic sources. This choice isn't a limitation of technology. In real-world applications, dealing with polychromatic sources involves the same approach; we only need to compute the diffraction at several wavelengths and express the final image irradiance through quadrature summation. However, in practice, monochromatic calculations remain relevant when the filters have a bandwidth of approximately 100 nm or less. Baudat and Hayes have demonstrated that the technique shows very good agreement when compared with a traditional interferometric approach [3].

First, we will outline the methodology with some results from its application for telescopes. Following this, we will describe its application in the context of the PSM. Finaly we will discuss the measurement of aspherical surfaces showing results using a PSM.

2. METHODOLOGY

2.1 AI4Wave background and concept

The far field, intensity distribution of the monochromatic point spread function (PSF) is proportional to the square modulus of the two-dimensional Fourier transform of the complex pupil function:

$$\mathrm{PSF}(u, v) \propto |\mathcal{F}_{2D}\{(\mathrm{P}(x, y)\}|^2 \tag{1}$$

The complex pupil function $\mathrm{P}(x, y)$ contains information about the shape of the pupil, the transmission function and optical phase in the pupil. In general, the complex pupil function is defined as follows:

$$\mathrm{P}(x, y) = \mathrm{p}(x, y)e^{j\varphi_p(x,y)} \tag{2}$$

where: $\mathrm{p}(x, y)$ = pupil amplitude transmission function,
$\varphi_p(x, y)$ = the pupil phase function = $2\pi W(x,y)/\lambda$, and
$W(x,y)$ = wavefront departure from the reference sphere.

With the required scaling factors, the radial PSF becomes:

$$\mathrm{PSF}(r') = \frac{I_0}{(\lambda f)^2}|\mathrm{T}(\rho)|^2_{\rho=r'/\lambda f} \tag{3}$$

Where:

I_0 = the irradiance in power/area incident on the pupil,
λ = operating wavelength,
f = focal length,
r'= radial coordinate in the focal plane,
$\mathrm{T}(\rho) = \mathcal{F}\{\mathrm{P}(r)\}$ = Radial Fourier transform (Hankel transform) of the complex pupil function.

Using Equation (3), the monochromatic PSF for any pupil phase distribution can be readily computed. Baudat [2] demonstrated the normalization and sampling of input data for broad applicability across optical systems.

Radial annular Zernike polynomials construct a selective orthogonal set of aberrations tailored for specific tasks. For example, in aligning two-mirror telescopes, minimizing on-axis coma and balancing off-axis astigmatism optimize secondary mirror alignment, while reducing spherical aberration optimizes mirror spacing. Identifying astigmatic and trefoil terms enhances field performance and detects mechanical mounting stress. Training the NN to recognize the nine Zernike terms in Table 2 suffices for these tasks. This method can extend to higher-order Zernike terms including atmospheric turbulence modelization (Kolmogorov and Von Karman theories). AI4Wave has been used successfully for

Zernike polynomials up to the 8th radial order. Generally, the piston term (z0=0) can be ignored, while tilt/tip (z1=0, z2=0) can disregarded by centering the defocused image during preprocessing before NN input.

Name	**Index**	**Radial Annular Polynomials** $0 < r \leq 1 \qquad 0 < \epsilon \leq 1 \qquad 0 \leq \theta \leq 2\pi$
Defocus	Z_3	$(2r^2 - 1 - \varepsilon^2)/(1 - \varepsilon^2)$
Vertical astigmatism	Z_4	$\left(r^2/\sqrt{1+\epsilon^2+\epsilon^4}\right) cos(2\theta)$
Oblique astigmatism	Z_5	$\left(r^2/\sqrt{1+\epsilon^2+\epsilon^4}\right) sin(2\theta)$
Horizontal coma	Z_6	$[3r^3(1+\epsilon^2) - 2r(1+\epsilon^2+\epsilon^4)]/\left[(1-\epsilon^2)\sqrt{(1+\epsilon^2)(1+4\epsilon^2+\epsilon^4)}\right] cos(\theta)$
Vertical coma	Z_7	$[3r^3(1+\epsilon^2) - 2r(1+\epsilon^2+\epsilon^4)]/\left[(1-\epsilon^2)\sqrt{(1+\epsilon^2)(1+4\epsilon^2+\epsilon^4)}\right] sin(\theta)$
Primary spherical	Z_8	$(6r^4 - 6r^2(1+\epsilon^2) + 1 + 4\epsilon^2 + \epsilon^4)/(1-\epsilon^2)^2$
Oblique trefoil	Z_9	$\left[r^3/\sqrt{1+\epsilon^2+\epsilon^4+\epsilon^6}\right] cos(3\theta)$
Vertical trefoil	Z_{10}	$\left[r^3/\sqrt{1+\epsilon^2+\epsilon^4+\epsilon^6}\right] sin(3\theta)$
Secondary spherical	Z_{15}	$[(20r^6 - 30r^4(1+\epsilon^2) + 12r^2(1+3\epsilon^2+\epsilon^4) - (1+9\epsilon^2+9\epsilon^4+\epsilon^6)]/(1-\epsilon^2)^3$

Table 1. Definition of the nine annular Zernike terms using the Wyant-Creath [8] numbering convention, following Mahajan's definitions. These are the basic common terms used for generating synthetic data and for training the AI system described here with $\varepsilon = 0$ for the PSM experiments.
In some context higher orders terms have been considered up to the Zernike radial order 8.

2.2 Data generation and training

The synthetic data, specific to a given optical imaging system (such as a telescope or a PSM), is computed using scalar diffraction theory and Fast Fourier Transform (FFT) to model the defocused image. For obstructed circular entrance pupils, we utilize the central obstruction parameter, denoted as $0<\varepsilon\leq1$. This parameter relates to the degree of obstruction as a percentage of the pupil diameter, D. This concept becomes particularly significant when evaluating a centered circular secondary mirror in the context of a telescope. Although this paper focuses on circular apertures (axially symmetric systems), the most common type, other shapes can also be accommodated.

We have chosen to use the Zernike radial annular polynomials for articulating the WF phase errors across the pupil. In relevant scenarios, we also consider the Fried parameter or coherence length (r0) for quantifying the strength of Earth's atmospheric turbulences, often referred to as 'seeing.' Various levels of noise are incorporated into the synthetic data to account for sensor, electronic, and shot noise, as well as scintillation.

To train the ANN, we generate defocused images across predefined ranges of the Zernike coefficients, in accordance with the application and aberration budgets, as well as r0 values where applicable. Alternate strategies could involve directly sampling an aberrated wavefront, with the NN outputting the sampled wavefront itself rather than Zernike coefficients or other aberration terms. In this paper, we adopt a parametric approach, describing the wavefront error using Zernike radial annular polynomials. For aspherical surfaces we would add more parametric description, such as conic constant and aspherical expansion coefficients.

The NN training phase employs three datasets:

a) Learning Dataset: Used to optimize NN synaptic weights, typically the largest set, ranging from 500,000 to several million of samples or more.
b) Validation Dataset: Monitors NN generalization performance during training to prevent overfitting, containing typically 10,000 to 50,000 samples.
c) Test Dataset: Assesses the model's post-training generalization capability, performance, bias and accuracy. All datasets are generated from identically distributed uniform random variable simulations, spanning the range of Zernike coefficients.

Figure 2 illustrates the basic steps involved in loading and training the neural network.

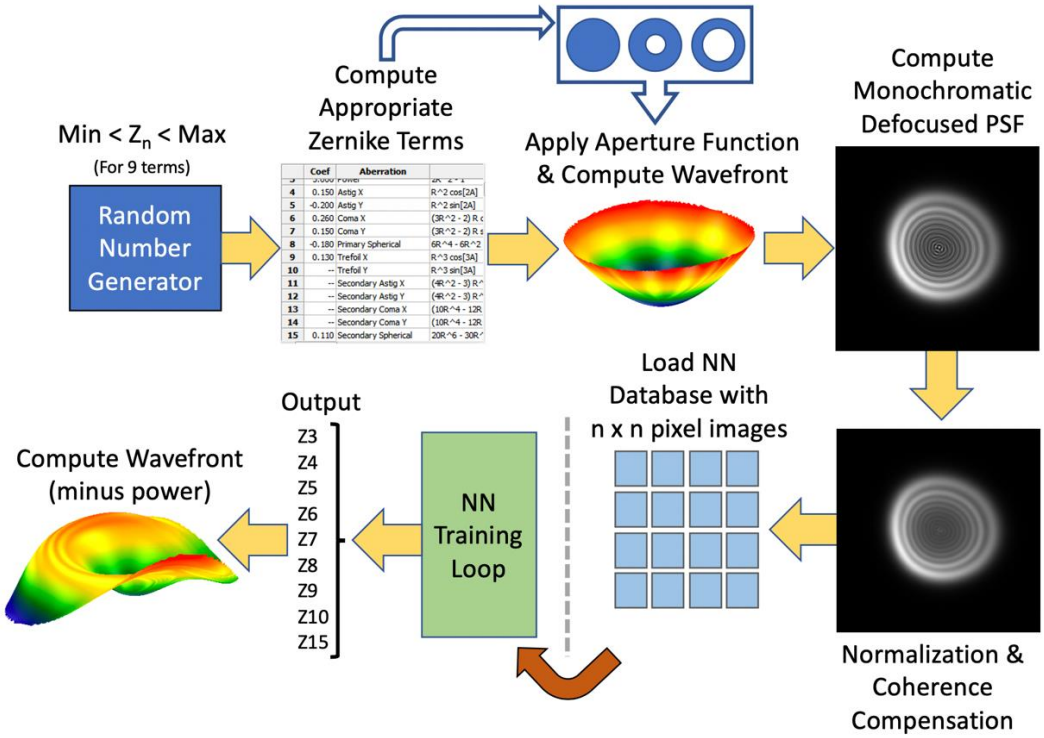

Figure 2. The basic steps for loading data and training the neural network (NN) to recognize 9 Zernike terms.

2.3 Uniqueness of phase retrieval

Beside piston (z0) and the spatial shifts tilt and tip (z1, z2), which all are set to zero in our application, phase retrieval faces a last trivial ambiguity, the conjugate inversion, as shown from the pupil function $P(x, y)$ cross-correlation, the OTF:

$$OTF(\zeta, \eta) = P(x, y) \otimes P(x, y) = P^*(-x, -y) \otimes P^*(-x, -y) \quad (4)$$

Where * denotes the complex conjugate operation.
There are 2 pupil functions $P(x, y)$ leading to the same PSF:

$$P(x, y) = p(x, y)e^{j\varphi_p(x,y)} \quad (5)$$
$$P^*(-x, -y) = p(-x, -y)e^{-j\varphi_p(-x,-y)} \text{ conjugate inversion} \quad (6)$$

For a circular pupil p(x,y) is a real even function, the only ambiguity we have to handle is for the phase $\varphi_p(x, y)$. This

issue can be tackled by introducing a known phase modulation. The most straightforward and simplest method involves adding a defocus bias (Z3). While other types of modulation, such as spherical aberrations, could be used, and are more relevant for aspherical surfaces.
Figure 3 shows a perfect PSF (left), and aberrated PSFs with +3 waves (center) and -3 waves (right) of primary spherical (Z8) aberration. The top row depicts the in-focus state (z3=0) with no phase modulation, where the two aberrated PSFs appear identical, indicating a loss of phase sign. This ambiguity is resolved here by adding a 10-wave defocus (Z3) bias as modulation, as seen in the bottom row, where the aberrated PSFs are distinguishable. A significant defocus bias ensures some degree of defocus with a known sign, accounting for defocusing bias accuracy, field curvature, sensor tilts, and other defocus errors. Unlike curvature sensing, we do not need to be beyond the caustic region to recover the wavefront. Any defocus error is treated as an aberration, and the NN is trained within a predefined range of defocus errors.

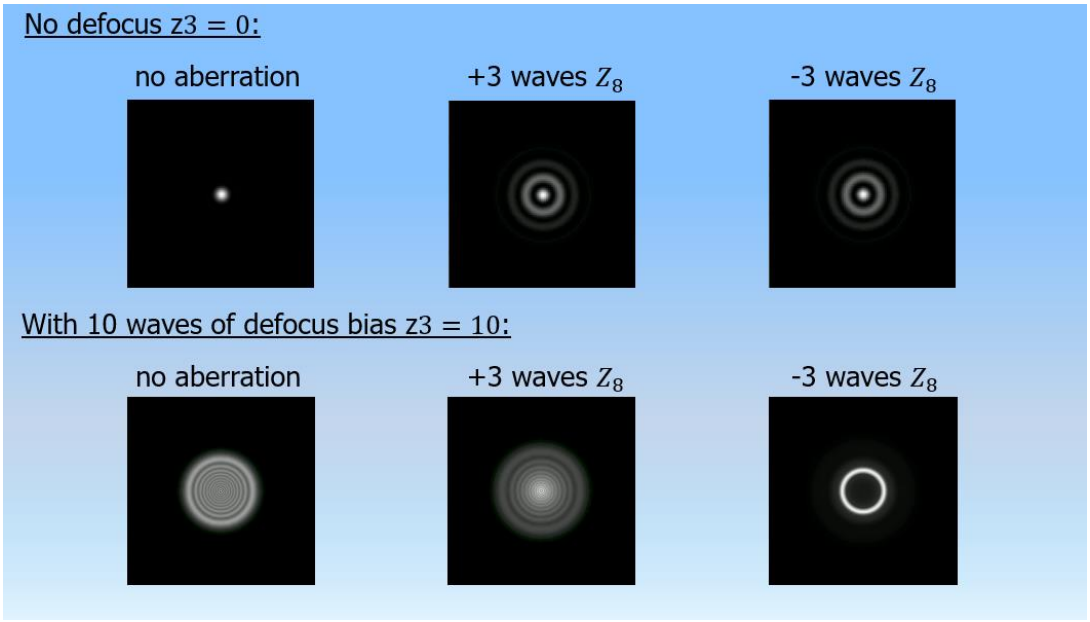

Figure 3. The top row corresponds to the in-focus situation (z3=0) with no phase modulation. The two aberrated PSFs, with respectively +3 (center) and -3 (right) waves of primary spherical (Z8), are identical, indicating that the phase sign has been lost. This ambiguity is resolved by adding 10 waves of defocus (Z3) bias, serving as the modulation, as observed in the bottom row.

In IS-WFS, besides piston, all useful phase information, including roughness, is indeed contained in the defocused image.

3. EXPERIMENTS WITH TELESCOPES

Several experiments have been carried out in the lab in double pass, and on the sky using real stars under seeing limited conditions [3]. Here, we present selected results obtained under laboratory conditions as an illustration. For additional results, please refer to [3].

3.1 Comparison with a Shack Hartmann wavefront sensor on an optical bench

A compact refractor telescope (Figure 4) with a pellicle beam splitter and a pinhole at the focal plane (serving as an artificial star) has been assembled. Defocused PSF images are captured by a CMOS camera with a red filter for near monochromatic modeling. The telescope, featuring a 24mm aperture and 300mm focal length (f/12.5), uses a white LED and diffuser to illuminate the pinhole.
For double-pass measurements, a flat mirror is positioned in front of the aperture. The CMOS camera can be swapped for a 40x40 lenslet SH wavefront sensor from ALCOR SYSTEM, maintaining consistent conditions with the same light source and red filter. SH sensor exposure is set at 200ms for adequate SNR, and AI4Wave CMOS camera exposure is set at 10ms,

suitable for video rate and AO applications.

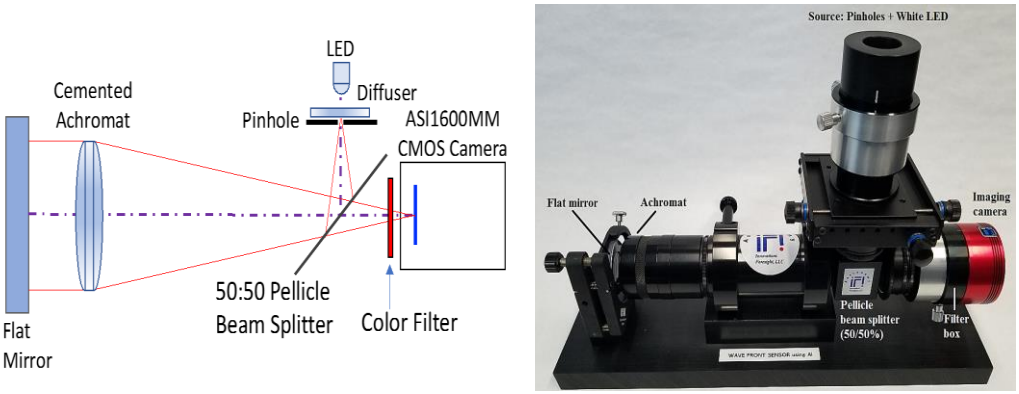

Figure 4. 24mm f/12.5 double pass refractor telescope with a pinhole, as an artificial star, and its CMOS camera

The table 2 shows the Strehl's ratio (SR), the WF errors, as well as the Zernike coefficients for the SH and the AIWFS approaches @650nm. They are in very good agreement, the maximum difference on the Zernike coefficient is 0.002 wave, or 1.3nm for astigmatism and secondary spherical.

Measurements (Zernike: Wyant's index)	**Shack-Hartman**	**AI4Wave**
Strehl's ratio (SR)	0.9864	0.9869
RMS FW error	0.017 wave (11.2nm)	0.018 wave (11.7nm)
PV FW error	0.127 wave (82.2nm)	0.116 wave (75.4nm)
Primary Astigmatism Z4+Z5	0.039 wave (25.0nm)	0.041 wave (26.7nm)
Primary Coma Z6+Z7	0.002 wave (1.5nm)	0.003 wave (2nm)
Primary Trefoil Z9+Z10	0.005 wave (3.5nm)	0.006 wave (3.9nm)
Primary Spherical Z8	0.002 wave (1.4nm)	0.002 wave (1.3nm)
Secondary Spherical Z15	0.021 wave (13.4nm)	0.019 wave (12.4nm)

Table 2. Comparisons on a refactor telescope optical bench between a SH WF sensor and the AI4Wave approach @650nm (monochromatic model)

4. POINT SOURCE MICROSCOPE FOR SURFACE MEASUREMENTS

4.1 Description and concept

The Point Source Microscope (PSM) is an autostigmatic microscope (AM) that also functions as an autocollimator and a reflection type inspection microscope [5]. The PSM is used primarily for the alignment of optics by precisely locating the centers of curvature of optical surfaces with a lateral resolution < 1 μm. When the PSM is focused at the center of curvature of a surface or optical system it simulates the use of an interferometer in a double pass test, the only difference being the PSM images the very small focal spot while the interferometer images the pupil of the surface being tested. The light path of the PSM focused at the center of curvature (CC) of a sphere is shown in the Figure 5.

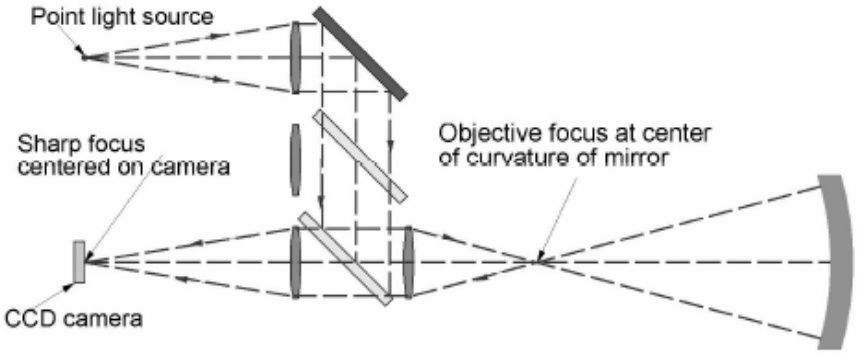

Figure 5. Light path in the PSM focused at the center of curvature of a spherical mirror to show the similarity with a double pass interferometer test setup

Given that the optical setup is similar to an interferometer, it made sense to explore the use of the PSM as a WF sensor for surface measurement in double pass. This can be achieved by simply adding a software module that implements AI4Wave technology. The module is designed as a Windows OS DLL, providing a generic way to integrate AI4Wave technology with various software and systems, including the PSM. Using the PSM offers at least two significant optical advantages over an interferometer, in addition to hardware and cost benefits. First, in scenarios where minimizing aberrations is the only feasible method of alignment—such as aligning a parabola to a return flat mirror—this setup is ideal. Traditional methods involving centers of curvature and foci are impractical in these cases. Second, if a surface is distorted during assembly, the ability to measure the WF effect during alignment allows for corrective action. This prevents discovering defects during final testing, thereby avoiding scrapping or reworking the assembly.

4.2 PSM and AI4Wave

With the PSM, the illumination originates from the free space end of a single-mode optical fiber which acts as a point source. This creates a Gaussian intensity distribution with a Numerical Aperture (NA) of 0.1, incident on a collimating lens with a 30 mm effective focal length (efl), resulting in a beam waist of 3mm. The lens is stopped at 8mm, leading to a truncated Gaussian beam. This variation in illumination implies that the NN must be trained for this case.
This creates a collimated beam, or plane wave, inside the PSM. This beam is transformed into a spherical wavefront by an infinite conjugate microscope objective placed on-axis at the center of curvature of a spherical or aspherical surface. The return beam is then focused onto the PSM camera. A mechanical spacer can be added to defocus the image based on the chosen AI4Wave defocus bias and the related PSM tube lens f-number (f/#), which is used to focus the return beam on the camera sensor. Equation 7 outlines the necessary spacing S for this approach.

$$S = B16\sqrt{3}\lambda f\#^2 \tag{7}$$

In Equation (7), B represents the defocus bias or the phase modulation, λ represents the wavelength, and f# denotes the f-number of the imaging optics (the PSM tube lens in this case). For the PSM, we set λ at 640nm and f# at 12.5 (tube lens's minimum f# when the PSM is the system stop). Assuming a AI4Wave model with a defocused bias of 3 wave rms (a design choice), that leads to a spacing of 8.314mm

Alternatively, the defocus can be conveniently created by adjusting the PSM's proximity to the test surface, generating a defocus bias aligned with the AI4Wave expectations. The degree of adjustment needed depends on the focal length or magnification of the microscope lens in use. In most case we usually want to overfill the surface under test such the surface determines the system stop and therefore the effective f/# of the PSM tube lens and the light cone reaching the camera. The PSM - initially focused at the surface's on-axis center of curvature (CC) - is shifted away through axial translation by a certain small ΔZ distance, in either direction. For small translations, there's a simple relationship outlined in Equation (8) between ΔZ and the motion of the image plane ΔI on the PSM's camera side.

$$\Delta \mathrm{I} = 2\left(\frac{\mathrm{f\#}_t}{\mathrm{f\#}_0}\right)^2 \Delta \mathrm{Z} \tag{8}$$

Where $\mathrm{f\#}_t$ represents the PSM's tube lens f-number which images the beam onto the camera. If the surface under test is overfilled and therefore becomes the system stop the value $\mathrm{f\#}_t$ must be calculated accordingly. $\mathrm{f\#}_0$ refers to the f-number of the PSM's microscope objective illuminating the surface under test. If the PSM is moved closer to the mirror, this results in an intra-focal defocused image.
Using the above example with a $\mathrm{f\#}_t = 12.5$ (the PSM being the system stop) and for a microscope objective NA=0.1, in the air, $f\#_o = 5$, resulting to a $\Delta \mathrm{Z} = \frac{8.314}{2}\left(\frac{5}{12.5}\right)^2 = 0.665\mathrm{mm}$ for 3 wave rms of defocus bias ($\Delta \mathrm{I} = 8.314\mathrm{mm}$, see above). This approach offers a unique, compact, and cost-effective solution for obtaining quantitative data on WFs and surface in double pass, thereby eliminating the need for an interferometer or dedicated wavefront sensors.

4.3 Measurements of aspherical surfaces

When measuring an aspherical surface with a PSM, the return beam's departure from a spherical wave needs to be modeled accurately to train the AI4Wave's neural network. The corresponding optical path difference (OPD) from the spherical wave translates to the same OPD for the internal return plane wave, which is eventually imaged onto the PSM's camera, with appropriate defocus, by the PSM tube lens. The aspherical surface's sag can be described generally as the sum of a base conic surface plus an expansion of the non-zero positive integer powers of the field radius r (distance from the optical axis), as shown by equation (9).

$$\mathrm{sag(r)} = \frac{\frac{r^2}{R}}{1+\sqrt{1-(K+1)\frac{r^2}{R^2}}} + \sum_{m=1}^{M} \propto_m r^m \tag{9}$$

Where R is the surface's curvature radius along the optical axis (on-axis), K the surface's conic constant, $\propto_m$ the aspheric coefficients and M the number of terms of the expansion. By definition, aspherical surfaces are axis-symmetrical. To compute the necessary defocused image seen by the PSM's camera using scalar diffraction theory, it is essential to define the wavefront departure ΔW_n, or wavefront nominal aspherical error, from the PSM's spherical wave due to the aspherical surface nominal prescription (equation (9)). In this paper ΔW_n, as well as any wavefront errors, is expressed in wave and in the context of a double pass test. ΔW_n is given by the equation (10) as a function of the normalized field radius $\rho = \frac{2r}{D}$ with D the diameter of the asphere fully illuminated by the PSM, or equivalent setup.

$$\Delta W_n(\rho) = \frac{1}{\lambda}\left[\frac{D\rho^2}{4f\#_s+\sqrt{16f\#_s^2-(K+1)\rho^2}} + 2\sum_{m=1}^{M} \propto_m \left(\frac{D}{2}\rho\right)^m - \frac{D\rho^2}{4f\#_s+\sqrt{16f\#_s^2-\rho^2}}\right] \tag{10}$$

In (10) we have introduced $f\#_s = \frac{f_s}{D}$ the f-number of the aspherical surface under test illuminated by the PSM's spherical wave from its microscope objective. $f_s = \frac{R}{2}$ is the aspherical surface focal length on-axis (R is the surface's curvature radius). Therefore $f\#_s$ is also given by $f\#_s = \frac{R}{2D}$. Since we want to measure the quality of the surface under test, we must also consider the departure from the nominal aspherical surface's figure. The related wave front error ΔW_e is a function of ρ but also of course the azimuthal angle θ. The equation (10) provides a general description of such error (in wave and in a double pass context).

$$\Delta W_e(\rho,\theta) = \frac{1}{\lambda}\left[\frac{\Delta K D \rho^4}{2\left(4f\#_s+\sqrt{16f\#_s^2-(K+1)\rho^2}\right)^2\sqrt{16f\#_s^2-(K+1)\rho^2}} + 2\sum_{m=1}^{M}\Delta_{\propto_m} m \propto_m \left(\frac{D}{2}\right)^m \rho^{m-1} + 2\sum_{n=2}^{N} z_n Z_n(\rho,\theta)\right] \quad (11)$$

Where ΔK is the error on the conic constant, $\Delta_{\propto_m}$ the error on the aspheric coefficients and z_n the Zernike coefficients for the associated polynomials $Z_n(\rho,\theta)$ using the Wyant-Creath [8] numbering convention. N is the index of the last Zernike polynomial used in the expansion. The wavefront error contribution from errors in ΔK and $\Delta_{\propto_m}$ has been calculated from the partial derivatives of equation (10) and is therefore only valid for small values, which is expected in most practical applications. The Zernike expansion is used to account for azimuthally dependent surface errors. Since axis-symmetrical errors are already encoded by the partial derivatives of the aspheric power expansion, all purely radial Zernike coefficients should be set to zero (ignored) to avoid over-determination.
Alternatively, the effects of aspheric coefficient errors can be encoded using the purely radial Zernike coefficients, ignoring the aspheric power expansion. These coefficients are related to balanced spherical aberrations of various orders and can be reconciled later with each $\Delta_{\propto_m}$ by simply identifying the aspheric power expansion with the Zernike expansion.
The total wavefront error $\Delta W_{total}(\rho,\theta)$ given by equation (12) is used to build the samples for training the AI4Wave NN assuming some ranges for each of the parameters $\Delta K, \Delta_{\propto_m}$ and z_n. Here, we considered that the aspherical surface on-axis radius R can be measured using the traditional PSM method [5] (from the cat's eye reflection) and can be therefore used to compute $f\#_s$, when needed. Partial derivative of equation (10) relative to small error on R could be considered if necessary too.

$$\Delta W_{total}(\rho,\theta) = \Delta W_n(\rho) + \Delta W_e(\rho,\theta) \quad (12)$$

4.4 Measurements of a parabola

A known parabola ($K = -1$) was placed in front of the PSM for measurement of its surface using the AI4Wave method. The parabolic surface is of very high quality ($\frac{\lambda}{50}$) while the PSM and its microscope objective exhibit a wavefront error of 0.035 waves RMS, attributed to a degree of coma and some astigmatism from mainly the internal beam splitters. Although the PSM's wavefront error could be of course subtracted (calibrated) from the measured error, this calibration was omitted to show larger Zernike coefficients reported by the AI4Wave module. The parabola radius of curvature R, on-axis, is 900mm while its diameter D is 114mm.

The AI4Wave defocus bias B was set to 3 waves rms from the diffraction-limited PSF (minimum wave front error) on the PSM's camera sensor plane, this corresponds to a total of 4.65 waves rms away from the paraxial conjugate image plane when the parabola center of curvature is placed at the PSM's microscope objective focal plane. The PSM was moved until the corresponding AI4Wave model reported a defocus error close to zero, inside the AI4Wave parabola model defocus tolerance. The Figure 6 below shows the PSM software GUI after acquisition and AI4Wave processing of the parabola defocused image.

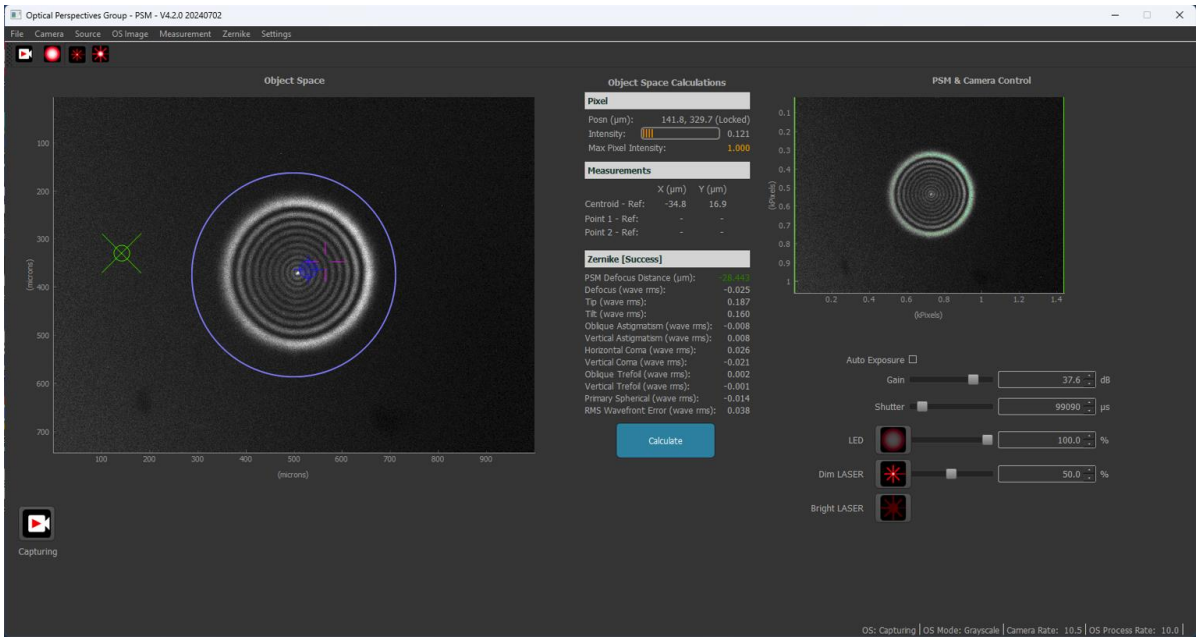

Figure 6. PSM software GUI: Measurement of a parabola with a total defocus of 4.65 wave rms from the parabola's center of curvature PSF (3 waves rms from the diffraction limited PSF).

The wavefront error measured by the PSM & AI4Wave is 0.038 wave rms (0.20 wave PV), essentially the aberrations from the PSM itself. The parabola contribution is only 0.003 wave rms, or 0.015 wave PV ($\frac{\lambda}{67}$). The Figure 7 shows side by side the measured defocused image (PSF) and the expected, perfect, defocused image (PSF) from the parabola (aberration free).

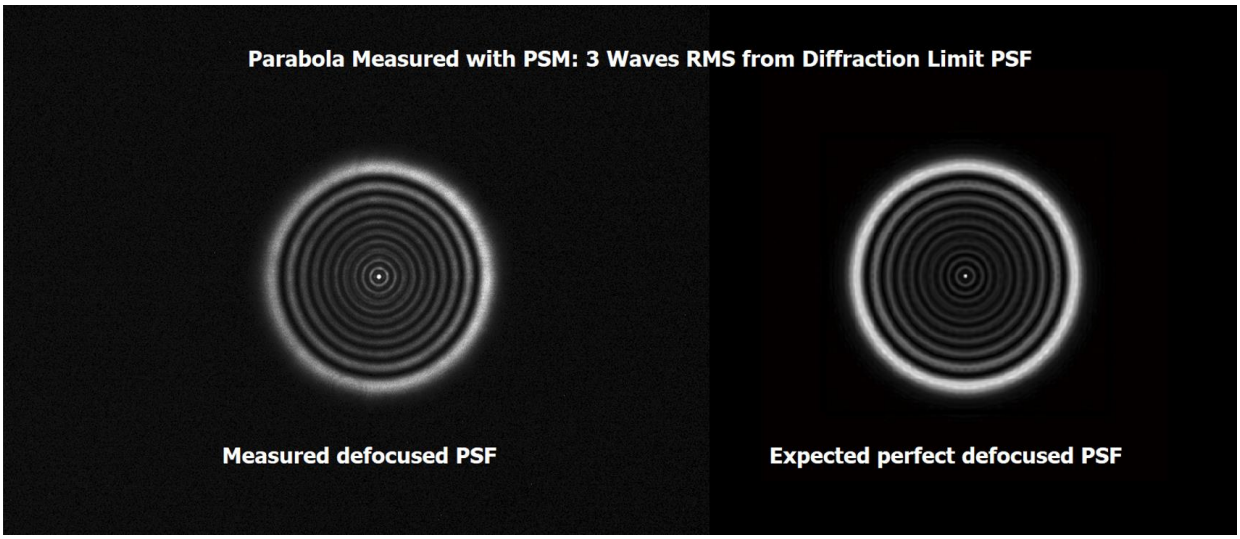

Figure 7. Left, measured (actual) defocused image (PSF). Right the theoretical perfect defocused image (PSF).

The last Figure 8 below shows the calculated double-pass fringes from the wavefront, representing the pattern that would be observed by an interferometer measuring the parabola without any null optics.

The PSM in this experiment uses a simple microscope objective without any additional dedicated optics. However, the

objective must capture the entire caustic. Even though the AI4Wave model can work with a very small defocus bias, it is essential to ensure that all the light returning from the aspherical surface is fully captured by the PSM.

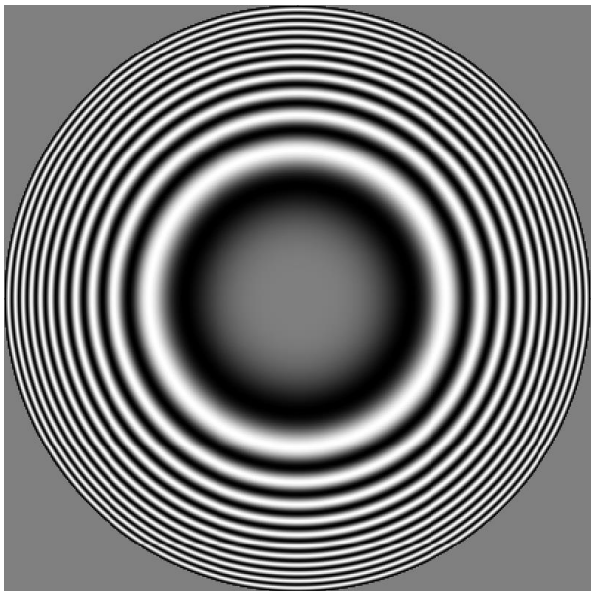

Figure 8. Calculated double-pass fringes from the wavefront

5. CONCLUSIONS

The AI4Wave method, tested with a PSM for aspherical surface measurement, uses Image Space Wavefront Sensing (IS-WFS) to compute wavefronts accurately. It employs a simple microscope objective, capturing full light from the aspherical surface without extra hardware. IS-WFS techniques, like phase retrieval, phase diversity, and curvature sensing, enable wavefront measurement directly from image data, avoiding specialized sensors but requiring runtime optimizations through iterative algorithms.

AI4Wave, on the other hand, leverages machine learning for IS-WFS to relate single image irradiance to wavefront phase quickly and accurately, eliminating time-consuming and potentially suboptimal iterative processes. This method provides a cost-effective, space-efficient, and precise solution for wavefront sensing. Combining PSM with AI4Wave offers a high-quality, minimal hardware approach for aspherical surface measurement, utilizing IS-WFS and machine learning.

REFERENCES

[1] Roddier Claude and Roddier Francois, “Wave-front reconstruction from defocused images and the testing of ground-based optical telescopes”, Journal of Optical Society of America, vol. 10, no. 11, 2277-2287 (1993).

[2] Gaston Baudat, “Low-cost wavefront sensing using artificial intelligence (AI) with synthetic data”, Proc. SPIE 11354, Optical Sensing and Detection VI April 1, Strasbourg, France (2020).

[3] Gaston Baudat and John Hayes, “A star-test wavefront sensor using neural network analysis”, Proc. SPIE. 11490, Interferometry XX, 20 August 5, San-Diego, USA (2021).

[4] Gaston Baudat, R. E. Parks, B. Anjakos, “A new approach to wavefront sensing: AI software with an autostigmatic microscope”, Proc. SPIE 12672, Applied Optical Metrology V, San-Diego, USA (2023).

[5] R. E. Parks and W. P. Kuhn, “Optical alignment using the Point Source Microscope”, Proc. SPIE, 5877, 58770B (2005)